Energy 305 (2024) 132216

Contents lists available at ScienceDirect

Energy

journal homepage: www.elsevier.com/locate/energy

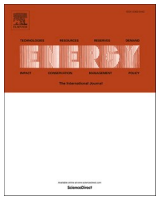

Effect of rear pyramid structures on industrial bifacial PERCs under omnidirectional incidence

Daxue Du [a], Dong Ding [a], Haibi Tang [a], Huanpei Huang [a], Feiyang Qiao [a], Chao Gao [a], Li He [a], Zhengping Li [a], Wenzhong Shen [a,b,*]

[a] Institute of Solar Energy, And Key Laboratory of Artificial Structures and Quantum Control (Ministry of Education), School of Physics and Astronomy, Shanghai Jiao Tong University, Shanghai 200240, PR China
[b] Collaborative Innovation Center of Advanced Microstructures, Nanjing 210093, PR China

ARTICLE INFO

Keywords:
Bifacial PERCs
Pyramid angles
Wavelength-dependent
Omnidirectional incidence
Bifacial gain

ABSTRACT

The bifacial passivated emitter and rear-side contact cells (PERCs) are capturing a growing photovoltaic market share, with a trend to replace monofacial device. Here, we reported five different rear pyramidal light trapping structures prepared by acid etching, with the monofacial counterparts as a comparison. The impact of the rear pyramid angles on the efficiency between under front and rear illumination shows an opposite trend due to a wavelength-dependent optical performance. To accurately optimize devices in real outdoor environments, the photovoltaic performance of mofacial and bifacial PERCs at different incident angles is simulated and integrated with an omnidirectional efficiency. Consequently, a significant improvement in bifaciality under omnidirectional incidence is obtained compared to vertical incidence, and a rough surface structure yields the maximum bifacial gain when the albedo is greater than 30 %. Furthermore, the power yield of monofacial and bifacial devices was predicted for every day in 2022.

1. Introduction

The p-type crystalline silicon (c-Si) passivated emitter and rear cells (PERCs) currently dominate the photovoltaic market due to low industrial cost and simple manufacturing process [1–3]. Another advantage of PERCs is that the fabrication of bifacial solar cells is fully compatible with existing production lines [4], thus the amount of consumed Al paste is dramatically reduced by up to 90 % and generate a higher open-circuit voltage (V_{OC}) [5]. Bifacial solar cells, compared with traditional monofacial devices, can absorb both the front incident light and the rear reflected light to generate electricity, thereby improving the energy output up to 30 % [6,7]. In 2022, shipments of bifacial photovoltaic modules have already reached 40 % in China [8], and the global market share of bifacial modules is projected to grow to almost 70 % by 2030 [9].

In 2015, Dullweber et al. [10] developed a new bifacial PERC solar cell design named PERC + that applies a screen-printed rear Al finger grid. The device obtained a front efficiency (η) of 20.8 % and a rear η of 16.5 %. Although an excellent bifaciality of up to 79 % for p-type cells was obtained with bifacial structured pyramids, the front η is not competitive compared to monofacial devices [11–13]. A planar rear surface was beneficial for monofacial PERCs [14,15] owing to an improved internal long-wavelength reflection and superior passivation property, but it was detrimental for rear light trapping in bifacial PERCs, resulting in low bifaciality [16]. With the popularity of bifacial PERCs, various studies were undertaken to improve the performance of bifacial PERCs [17–24]. Recently, Li et al. [21] proposed a gradient-designed capping layer to improve antireflection effect in the short wavelength, achieving a higher front η of bifacial PERCs than monofacial counterparts with the same rear planar surfaces. Meanwhile, by application of structured pyramids on both sides, Ma et al. [22] have reported the best front η of 23.42 % and a rear η of 17.13 % in bifacial PERCs. Nevertheless, a lower bifaciality of 74.5 % was obtained mainly due to the rear short-circuit current density (J_{SC}) loss.

Apparently, the rear surface morphology constraints the optical and electrical performance of bifacial PERCs. Therefore, Shen group [25] has investigated the impact of four different rear pyramid title angles based on acid solution etching on bifacial PERCs in 2020. The results

* Corresponding author. Institute of Solar Energy, and Key Laboratory of Artificial Structures and Quantum Control (Ministry of Education), School of Physics and Astronomy, Shanghai Jiao Tong University, Shanghai 200240, PR China.
E-mail address: wzshen@sjtu.edu.cn (W. Shen).

https://doi.org/10.1016/j.energy.2024.132216
Received 18 May 2023; Received in revised form 18 June 2024; Accepted 24 June 2024
Available online 25 June 2024

demonstrate a smaller decrease in the front η and a larger increase in the rear η, as the tilt angle of the rear pyramid increases. Hence, a highest front η of 22.57 % achieved for PERCs with a nearly planar rear surface, with a bifaciality of 74.7 %. Then, Ding et al. [26] derived a similar conclusion by six different rear pyramid structures using the same acid etching method. However, the preference of the rear structure is not sufficient only by the measured results with a same light power under vertical incidence, considering the actual solar motion. In addition, the bifacial gain between monofacial PERC and bifacial PERC with rear pyramid morphologies has not been concerned. Conversely, a large of simulations and experiments were conducted to confirm the advantages of bifacial solar cells, combining the effects of weather, albedo, temperature, installation angle, etc [27–34]. However, these efforts hardly focus on light trapping structures and utilize mature products available on the market, which restricts the applicability of the research results to guide the development of new photovoltaic devices.

In this work, we have investigated the optical and electrical correspondence with five rear pyramidal structures on industrial bifacial PERCs under front and rear illumination, with the monofacial cells featuring a rear planar structure as a reference. Performance discrepancies at different light incident angles were simulated in front and back light. In addition, the omnidirectional η was achieved by simultaneously introducing variations in incident angle and power to reevaluate the bifaciality and bifacial gain. Finally, the calculations were carried out to access the energy yield for every day of monofacial and bifacial PERCs in practical application.

2. Experiment and simulation

2.1. Fabrication of monofacial and bifacial PERCs

The schematic structure of the fabricated bifacial PERCs was shown in Fig. 1(a). The p-type silicon wafers with a size of 158.75 mm × 158.75 mm and a thickness of 180 μm were used in this work. The manufacturing process underwent the following steps on the production line: (1) RCA cleaning and wet chemical alkaline texturing were conducted to achieve a random pyramid structure, then underwent a diffusion (DS-300C, S.C.) with $POCl_3$ to form n^+ emitter with a sheet resistance (RSH) of 130 Ω/sq; (2) the highly doped n^{++} area was obtained by a laser-doping process (DR-AL-Y40, DR Laser) with a sheet resistance of 80 Ω/sq; (3) As shown in Fig. 1(b) the rear acid etching was performed on the original pyramids with mixed $HF/HNO_3/H_2O$ solution reported in our previous work [25]. In brief, the etching process started with the oxidation of Si to SiO_2 by HNO_3, followed by the dissolution of SiO_2 as a result of reacting with HF. The volume ratio of HF to HNO_3 solution was changed to lower the tilt angle of pyramids with an initial value of 55.2°, with detailed formula presented in Table 1.

After etching, the PSG layer was removed in HF solution, and the thermal oxidation process was carried out on the samples to form the SiO_2 layer; (4) 6 nm AlO_x layer was prepared by the atomic layer deposition (ALD, Ideal Energy) on the rear-side surface; (5) SiN_x films were deposited on the rear-side surface with a thickness of 85 nm by plasma-enhanced chemical vapor deposition (PECVD, PD-405C, S.C.) and (6) SiN_x films with a thickness of 75 nm were deposited on the front-side surface; (7) laser ablation (DR-AL-Y40, DR Laser) was conducted on the rear-side to obtain an opening contact; (8) screen-printing (Softline-DL-SP, Maxwell) was used for the metallization process. The rear-side of bifacial PERCs has applied an Al metal grid with a 9-busbar design.

2.2. Simulation of monofacial and bifacial PERCs

The impact of rear surface morphology on the optical performance of the monofacial and bifacial PERCs was simulated by the wave optic module of COMSOL 5.5 software [35,36]. Material properties and geometric structures are constructed in simulated models for reference to the prepared devices, as the schematic of the structured bifacial PERCs exhibited in Fig. 1 (b). The models are constructed on a perfect matching layer (PML), SiNx (75 nm) and SiO_2 (10 nm) as rear passivation layers, followed by c-Si as an active layer (170 μm), AlOx (6 nm) and SiNx (85 nm) as rear passivation layers. We utilized periodic boundary conditions on the left and right sides of the models to simplify the calculation. The standard AM 1.5G spectrum was introduced as the incident light source under both front and rear illumination, and the wavelength-dependent complex refractive indexes (N) [37–40] of the stacks were provided in Fig. S1, including refractive index (n) and extinction coefficient (k) as

Table 1
Acid etching formula for different rear pyramid angles.

$HF/HNO_3/H_2O$	polished	65/240/30	45/240/30	45/240/60	30/50/140
α (degree)	0	16.8	25.8	35.3	51. 1

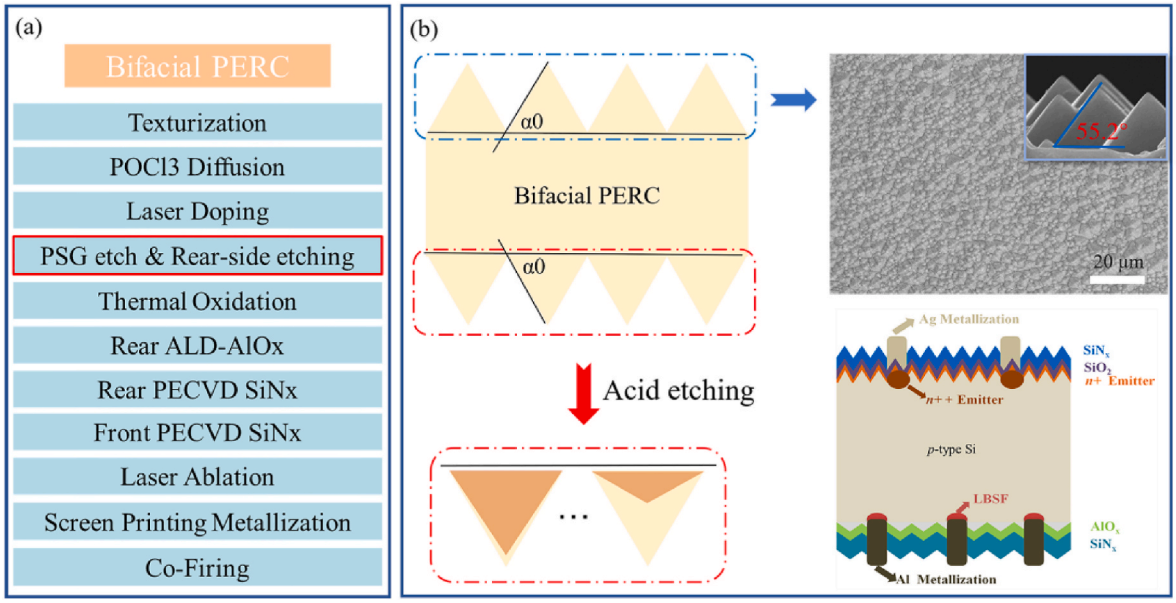

Fig. 1. (a) The industrial process for bifacial PERC. (b) Illustration of acid etching process on the rear-side to prepare different pyramid structures of bifacial PERCs.

follow.

$$N(\lambda) = n(\lambda) + ik(\lambda) \quad (1)$$

To simulate the influence of the rear pyramid structures on the optical properties, we defined the parameter α that represents the tilt angle of the pyramids, which is fitted to 0°, 16.8°, 25.8°, 35.3°, and 51. 1° of the rear side without considering the rounding effect.

In order to evaluate the energy output of bifacial PERCs with different rear pyramids for outdoor applications, the energy yield based on monofacial and bifacial PERCs has been further evaluated according to the cell efficiency and the daily solar irradiance spectra, which were extracted from solar spectrum on online PV lighthouse.

3. Results and discussion

3.1. Comparison between monofacial and bifacial PERCs

Fig. 2(a) distinguishes the structures of monofacial PERCs with a flat rear surface. The mass efficiency distribution of monofacial PERCs is shown in Fig. 2(b). Excluding individual products [17,21], the η displays a Gaussian distribution between 22.55 % and 23.05 %, with an average value of 22.83 %. The representative *J-V* curve of the monofacial PERC was drawn in Fig. 2(c), exhibiting a J_{SC} of 41.26 mA/cm^2, V_{OC} of 681.8 mV and fill factor (*FF*) of 81.15 %. The bifacial photovoltaic parameters were measured using a non-reflective black cloth on the other side when the illumination came from one side. Instead of the full area Al-BSF used in monofacial PERC, the rear-side of bifacial PERC has applied an Al metal grid in Fig. 2 (d). As exhibited in Fig. 2(e), the average η reaches 22.79 %, and 16.65 % under front and rear illumination, respectively. Compared to the monofacial one, the bifacial PERC obtains an extremely close η under front illumination, which results from the increase of V_{OC} on the one hand and the decrease of J_{SC} and *FF* on the other hand. Based on a similar front η, a net increase in rear power generation indicates why bificial solar cells are popular. A low η of the rear side is mainly attributed to a small J_{SC} due to the absence of a trapped light structure. Fig. 2(f) presents the measured *J-V* curves of bifacial PERC under front and rear illumination.

3.2. Impact of rear structures

The ability to light trap fundamentally affects the current generation and is highly dependent on the front and rear surface structures. Hence, the representative electric field intensity distributions at different pyramid angles are presented in Fig. 3. For the visualization of the pyramid structure, we have reduced the thickness of the Si wafer from the actual 170 μm to a modeled 20 μm. It can be observed from the electric field intensity in Fig. 3(a) that the rear pyramid structures provide a weak optical enhancement under front illumination since the light trapping effect is mainly determined by the same front surface. Considering the actual thickness of PERCs, the rear pyramids only contribute in the long wavelength range because the absorption coefficient (a) of the crystalline silicon here is sufficiently small to allow photons to reach the bottom [37] using Eq. (2).

$$a = \frac{4\pi k(\lambda)}{\lambda} \quad (2)$$

On the contrary, when light is under rear illumination, the photons need to reach the rear structure first. Hence, the electric field intensity in the pyramid structures is much higher than the surroundings under rear illumination as exhibited in Fig. 3(b), revealing the strong light-trapping effect of the rear pyramid structure. Moreover, this effect strengthens with the increased tilt angles.

To quantify the impact of the rear surface on optical performance, Fig. 4(a) exhibits the measured reflectance and external quantum efficiency (EQE) results illuminated from the front side in three characteristic wavelengths at 400 nm (short), 700 nm (middle) and 1000 nm (long). The effect of the rear surface is distinct in the long wavelength. Meanwhile, the performance in short and middle wavelengths is similar, and the reflection of planar samples exceeds that of the others significantly in the long wavelength. Reflection decreases with increasing α value. Interestingly, the EQE values exist an opposite variation compared to reflectance in the long wavelength but little change in the middle and short wavelength, which is induced by the discrepancy in the internal quantum efficiency (IQE) as follows.

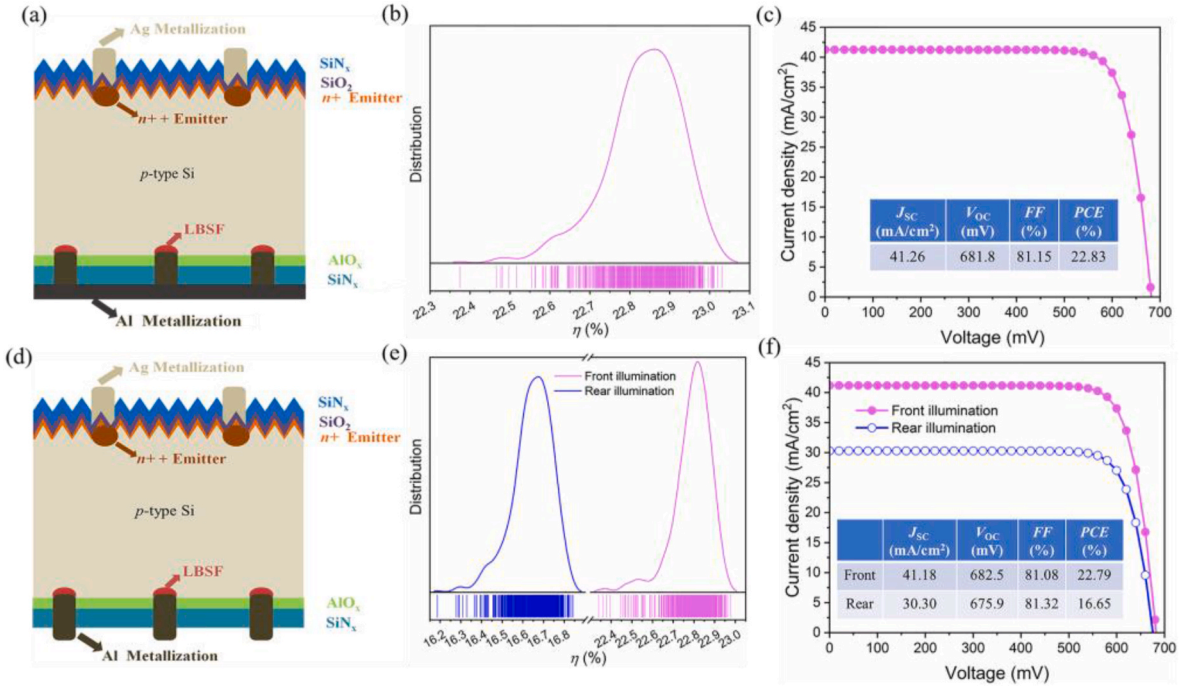

Fig. 2. Schematic structure, statistical distribution of η (800 cells for each group) and representative *J-V* curve corresponding to (a–c) monofacial and (d–f) bifacial PERCs.

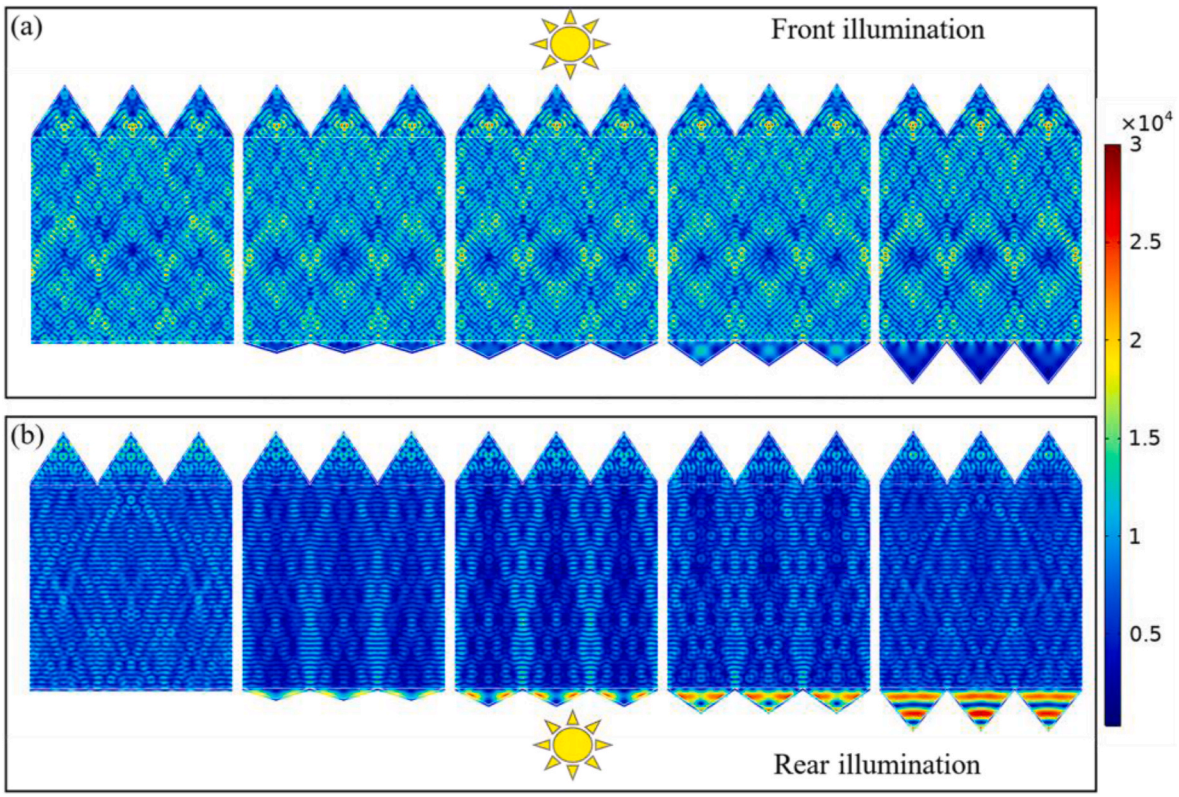

Fig. 3. Electric field intensity distributions of the bifacial PERCs at wavelength of 700 nm versus rear pyramid angles under (a) front and (b) rear illumination.

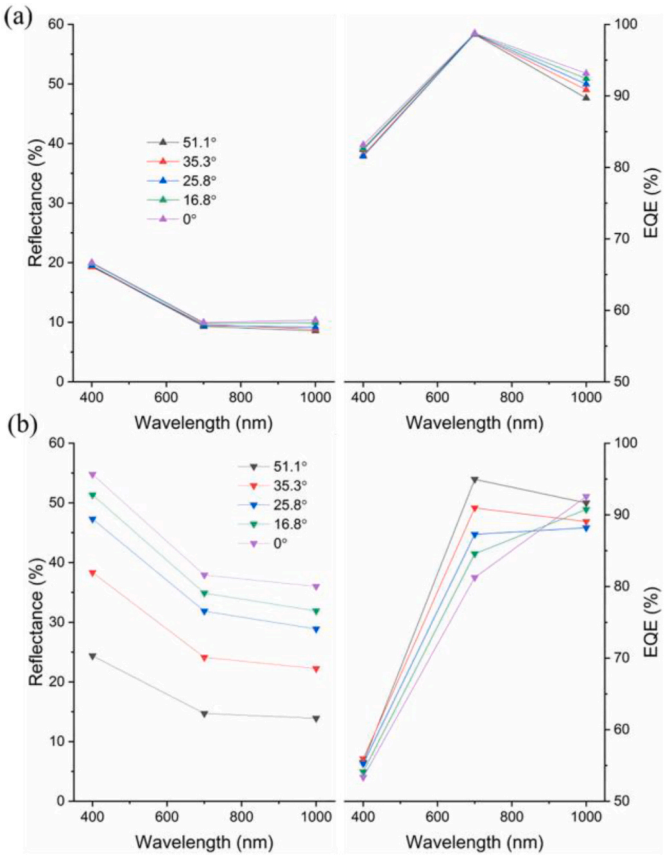

Fig. 4. Reflectance and EQE versus rear pyramid angles under (a) front and (b) rear illumination.

$$A(\lambda) = 1 - R(\lambda) - T(\lambda) \tag{3}$$

$$EQE(\lambda) = A(\lambda) \bullet IQE(\lambda) \tag{4}$$

Where λ is the wavelength of the incident light, R/T/A is reflectance/transmittance/absorption, respectively.

This indicates that the weak optical enhancement brought by the rear pyramids cannot compensate for the passivation loss under front illumination. The reflection and EQE performance when illuminated from the rear side was also assessed, as shown in Fig. 4(b). Reflection decreases significantly with increasing α, indicating more trapped photons and higher EQE. The EQE performance is inferior to that of Fig. 4(a) in the short and middle wavelength, improved significantly with the rising α. The above results demonstrate that superior optical performance was achieved with a rear pyramid under rear illumination.

The bifacial PERCs featuring different rear pyramid angles were developed to assess the impact of rear structures on photovoltaic performance. Fig. 5 presents the normalized average parameters under vertical front illumination using the planar PERCs as a standard. The J_{SC}, V_{OC}, *FF* and η all steadily decreases with the increased α value. The V_{OC} of PERCs with maximum α (51.1°) decays to 0.993 of the planar samples. The V_{OC} evolution brought about by the rear structure is unified whether the front or rear light. The smaller the rear roughness, the lower the surface recombination [41], thus higher the V_{OC} of PERCs.

Nevertheless, the J_{SC} exhibits an opposite regularity when the direction of light turns, reduced to 0.987 and raised to 1.061 with increasing α from 0 to 51.1°, respectively. Through Eq. (5), we can establish the relationship between J_{SC} and EQE. According to the preceding EQE analysis, it can be found that the difference of J_{SC} mainly comes from the middle wavelength region as well.

$$J_{SC} = \frac{q}{hc}\int_{\lambda_0}^{\lambda_g} \lambda EQE(\lambda)\varnothing(\lambda)d\lambda \tag{5}$$

Where q is the electron charge, Ø(λ) is the standard solar spectra.

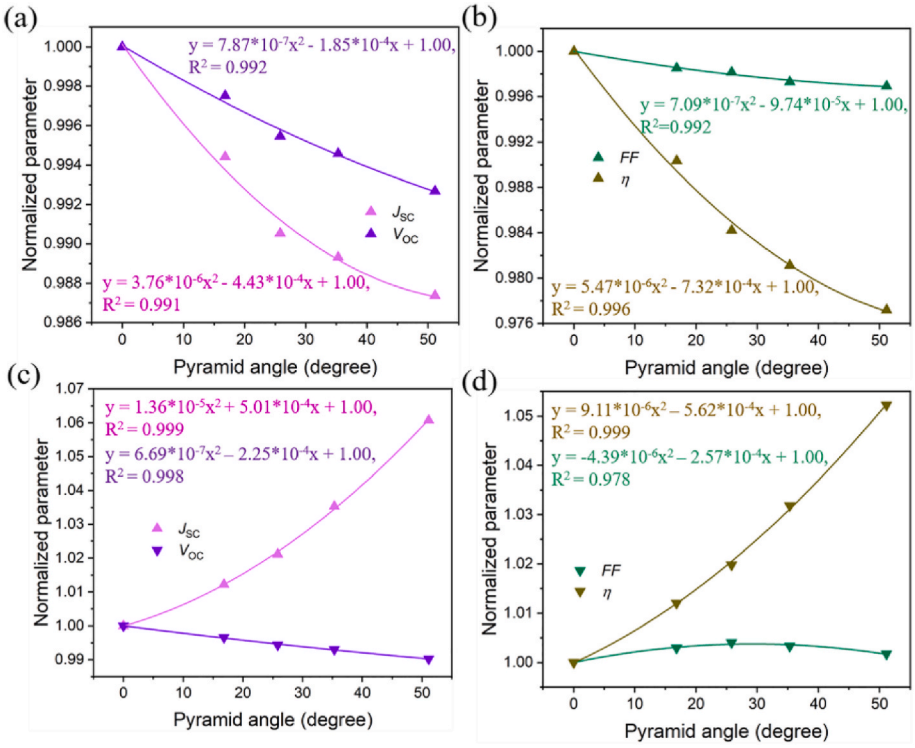

Fig. 5. (a–b) Front and (c–d) rear average parameters including V_{OC}, J_{SC}, *FF* and η of the bifacial PERCs (800 cells for each group) versus rear pyramid angles.

Meanwhile, the *FF* maintains high stability within 0.4 % fluctuation. According to Eq. (6), the change in η is determined by $J_{SC} \times V_{OC}$, with a fixed P_{in} of 1000 W/m^2 under test conditions.

$$\eta = \frac{P_{out}}{P_{in}} = \frac{V_{OC} \times J_{SC} \times FF}{P_{in}} \tag{6}$$

Where P_{in}/P_{out} represents the input/output power. Detailed parameters of bifacial PERCs versus rear pyramid angle α were listed in Table 2. To summarize, the rear pyramid with a large α results in a smaller loss of 0.023 in front η originated from damage from interfacial recombination and a larger improvement of 0.052 in rear η due to enhanced light absorption.

3.3. Impact of incident angle

Since the incident angle of sunlight in an outdoor environment varies throughout the day, simply comparing the parameter of PERCs under vertical incidence is not adequate to optimize the rear pyramid structures. Therefore, the omnidirectional performance of the PERCs was explored from 0° to 80° of incident angle θ, which was set to 0° corresponding to the normal incidence. To focus on the effect of θ variation, the J_{SC} calculated through Eq. (5) was normalized taking the results of 0° illumination as 1.

Table 2
Average normalized parameters of bifacial PERCs with different rear pyramid angles under front and rear illumination.

α (degree)		0	16.8	25.8	35.5	51.1
Front	J_{SC}	1	0.9944	0.9905	0.9893	0.9874
	V_{OC}	1	0.9975	0.9955	0.9946	0.9927
	FF	1	0.9985	0.9981	0.9973	0.9969
	η	1	0.9903	0.9984	0.9811	0.9772
Rear	J_{SC}	1	1.0122	1.0211	1.0353	1.0607
	V_{OC}	1	0.9966	0.9944	0.9930	0.9902
	FF	1	1.0030	1.0041	1.0033	1.0017
	η	1	1.0120	1.0198	1.0318	1.0523

As shown in Fig. 6(a), the increasing θ leads to an attenuation of the normalized J_{SC} when illuminated from the front side, and the effect among the rear pyramidal structures grows pronounced after 40° of incident angle. Compared to that of 0.895 with α of 0°, a slightly bigger 0.913 with α of 51.1° at an incidence of light reveals a faint impact of the rear structures for PERCs in J_{SC}. Furthermore, the η of the monofacial and bifacial PERCs were plotted in Fig. 6(b) at different θ. Interestingly, the η of different pyramid structures tends to be uniform with the θ rising, rather than diminishing sequentially by increasing α in the case of 0° incidence.

Similarly, the normalized J_{SC} and η of PERCs were exhibited in Fig. 6 (c–d) when illuminated from the rear side. The more inclined the light, the more prominent the contribution of the pyramidal angles to light absorption, as demonstrated by the normalized J_{SC} of 0.601 α of 0° and 0.912 with α of 51.1°. And the change in η is significantly consistent with J_{SC}.

In order to comprehensively evaluate the effect of different incident angles on photovoltaic performance, we defined the η (η_{omni}) of PERCs under omnidirectional incidence to accurately assess the actual impact of the rear structure.

$$\eta_{omni} = \frac{\int_0^{90} \eta(\theta) P_{in}(\theta) d\theta}{\int_0^{90} P_{in}(\theta) d\theta} \tag{7}$$

Fig. 7(a) shows the variation of sun incident power with zenith angle (i.e., θ) without considering the influences of weather. Consequently, with the increasing θ, η_{omni} of bifacial PERCs slowly reduces from 16.17 % to 15.93 % under front illumination, while improving from 12.55 to 13.74 under rear illumination. And the monofacial PERC maintains a front η_{omni} of 16.19 %, fractionally exceeding the bifacial ones.

In industrial production, bifaciality is an intuitive and vital indicator for bifacial solar cells, which can be obtained by Eq. (8).

$$Bifaciality = \frac{\eta_{rear}}{\eta_{front}} \times 100\% \tag{8}$$

Therefore, the bifaciality of devices under vertical and omnidirectional

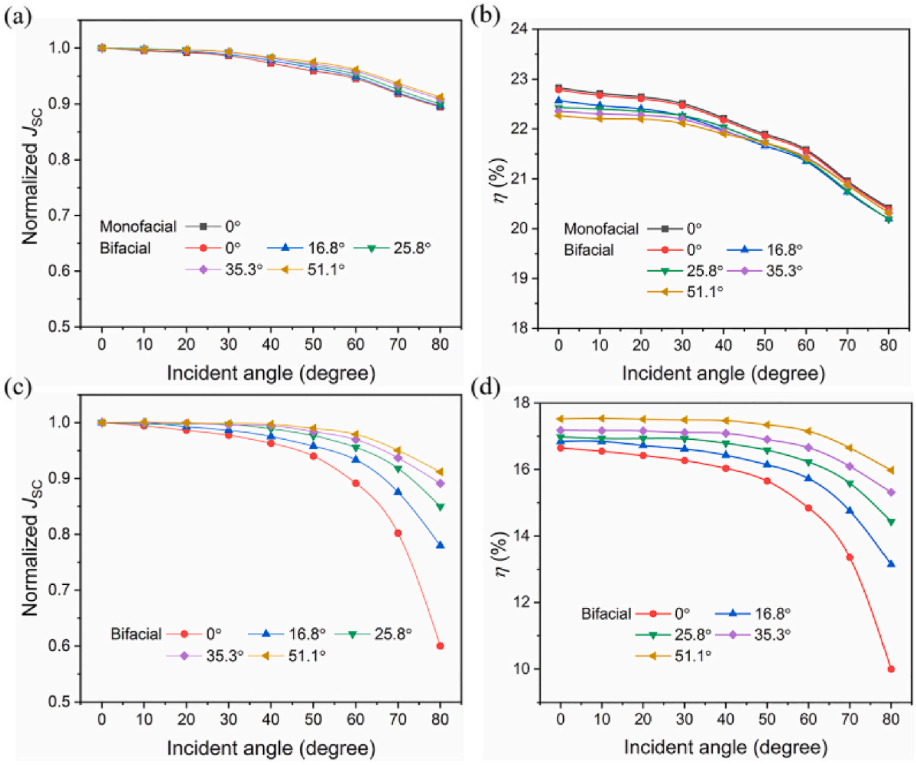

Fig. 6. Simulated (a–b) front and (c–d) rear parameters both normalized J_{SC} and η for the monofacial and bifacial PERCs.

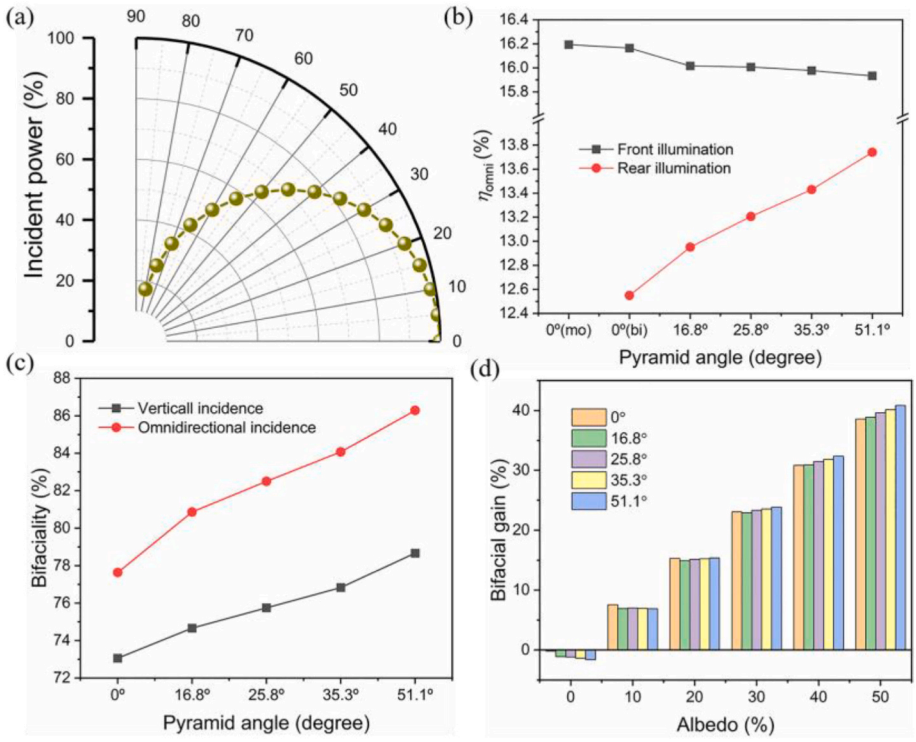

Fig. 7. (a) Incident light power versus zenith angle, (b) η_{omni} of monofacial PERC and bifacial PERCs versus rear pyramid angles, (c) the bifaciality of bifacial PERCs under vertical and omnidirectional incidence, (d) bifacial gain versus rear pyramid angles.

incidence was counted in Fig. 7(c). The omnidirectional conversion does not change the pattern of bifaciality evolving with the pyramid structures but boost the specific value of the same device. For example, a bifaciality of 73.06 % under vertical incidence was improved to 77.63 % under omnidirectional incidence, since the variation of the sunlight power was introduced into the comparison. Moreover, the enhancement was sequentially increased due to the excellent oblique light capture with a large α, reaching 4.57 %–7.62 %. Our findings correct the

recognition that the bificiality of bifacial PERCs is generally lower than 80 % [21], which can contribute to further exploiting the potential of PERCs.

However, the bifaciality cannot determine the contribution of the rear pyramids on photovoltaic performance due to simultaneous changes in front and rear η (see Fig. 6). The output power gain of the bifacial PERCs compared to the monofacial competitor was calculated as follow.

$$Bifacial\ gain = \frac{P_{bi}}{P_{mo}} - 100\% = \frac{\eta_{front} + \rho \times \eta_{rear}}{\eta_{mo}} - 100\% \quad (9)$$

Fig. 7(b) shows the calculated bifacial gain of output power for bifacial PERCs at different albedo, regarding the set with a monofacial device as a reference. The bifacial gain was expanded to analyze the impact of the incident angle in Fig. S2. The positive return can be generated for bifacial PERCs, only requiring an albedo of much less than 10 %. As the albedo increases to 30 %, the advantages gradually emerge of the α value of 51.1° to obtain the maximum gain, approaching 23.87 %. In summary, the bifacial PERCs with a planar rear surface are preferable when the ground albedo is lower than 20 %, while, a rough rear structure (α = 51.1°) is recommended under the albedo higher than 30 %.

3.4. Energy yield

The energy (E) yield based on monofacial and bifacial PERCs has been further evaluated using Eq. (10).

$$E = \int P_{out}(\theta)dt = \int P_{in}(\theta) \bullet \eta(\theta)\ dt \quad (10)$$

P_{in} with a specific zenith angle (θ) is obtained from the website of PV lighthouse [42]. We selected two representative cities in China, Shanghai (~121°E, 30°N) and Beijing (~116°E, 40°N), as examples to simulate for every day in 2022 under clear-sky conditions. The albedo was chosen to be 20 %, which is close to the typical values for photovoltaic modules installed on grounds, such as soil (15 %), grass (22 %), concrete (28 %), etc [5,43]. The daily energy yield of monofacial and bifacial PERCs with different rear pyramid angles were plotted in Fig. 8. The maximum and minimum energy yields were obtained in June and December of the year at both Shanghai and Beijing because these two cities are located at a similar longitude. Daily energy distribution in Shanghai for monofacial PERC is 1.035–2.389 kWh/m^2, while 1.194–2.756 kWh/m^2 for bifacial PERC with α of 51.1°. And they correspond to 0.707–2.456 kWh/m^2 and 0.815–2.833 kWh/m^2 in Beijing, respectively. It is reasonable to further assume that the further away from the equator, the greater the difference between peaks and valleys in power generation. The approximate energy outputs at 20 % albedo were achieved of bifacial PERCs, reaching about 743 kWh/m^2 in Shanghai and 673 kWh/m^2 in Beijing. The maximum yield was attained with α of 51.1°, followed by 0°, 35.5°, 25.8°, 16.8°, which is consistent with the trend observed in Fig. 7(d). Hence, by adjusting the albedo, the more differentiated energy yield of bifacial PERCs can be further regulated. Our results contribute to obtaining the maximum power yield from PERC cells tailored to real environments, which also allows the maximization of the economic efficiency of PV modules, according to the omnidirectional illumination.

4. Conclusions

In summary, we have fabricated monofacial PERCs with an average η of 22.83 % and five sets of bifacial PERCs with different rear structures using etching acid method. And the bifacial PERCs with a α of 0° achieved the highest front average η of 22.79 %. However, the rough surfaces led to a reduction up to 1 % in V_{OC} under rear illumination due to reduced passivation properties and increased interfacial recombination. On the other hand, the J_{SC} gain under rear illumination was significant,

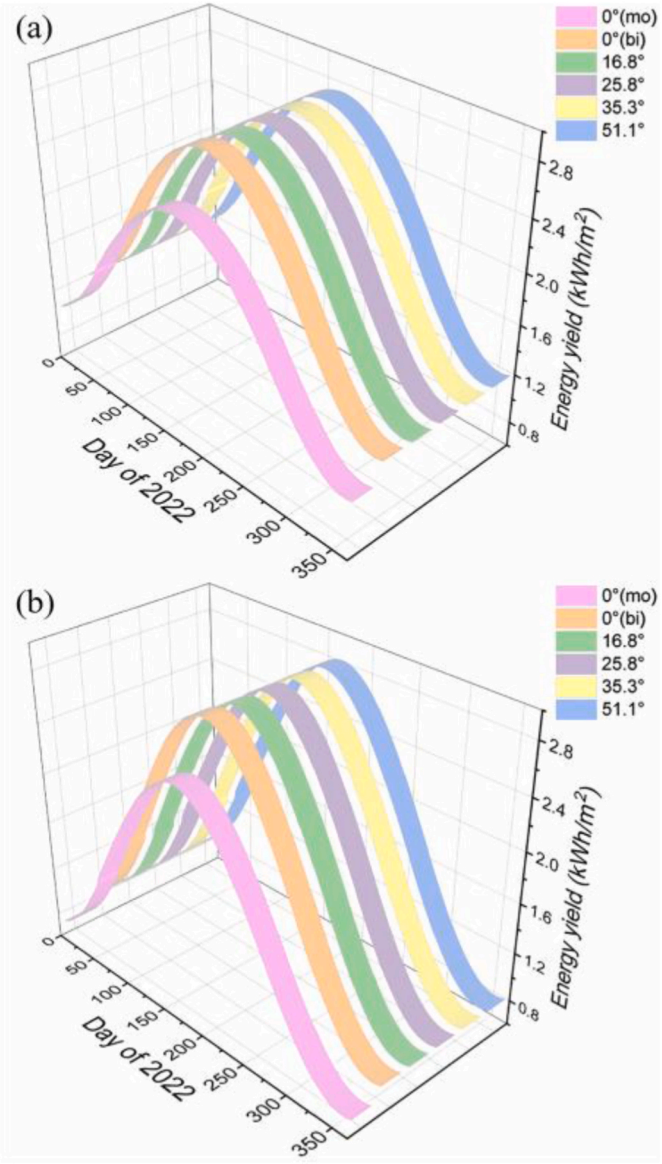

Fig. 8. Daily energy yield of monofacial and bifacial PERCs in (a) Shanghai and (b) Beijing versus rear pyramid angles.

leading to an increase in η. The simulated photovoltaic performance at different incident angles (θ) confirmed the superiority of trapped light with a large pyramid tilt angle (α). Therefore, an omnidirectional η was calculated to evaluate the bifaciality and bifacial gain of the device. Consequently, the bifaciality was enhanced by 4.57%–7.62 % based on omnidirectional incidence. We found that for the albedo exceeding 30 %, a largest rear pyramid angle (α = 51.1°) was optimal for achieving the output power, while for an albedo below 20 %, a planar rear surface was recommended. Finally, we predicted the daily energy yields for monofacial and bifacial PERCs located in Shanghai and Beijing. Our findings have significant implications for the development and practical applications of efficient bifacial photovoltaic devices.

CRediT authorship contribution statement

Daxue Du: Writing – original draft, Software, Methodology, Data curation, Conceptualization. **Dong Ding:** Software, Formal analysis. **Haibi Tang:** Investigation, Data curation. **Huanpei Huang:** Visualization, Conceptualization. **Feiyang Qiao:** Methodology, Investigation. **Chao Gao:** Supervision. **Li He:** Validation. **Zhengping Li:** Project

administration. **Wenzhong Shen:** Writing – review & editing, Resources, Funding acquisition.

Declaration of competing interest

The authors declare that they have no known competing financial interests or personal relationships that could have appeared to influence the work reported in this paper.

Data availability

Data will be made available on request.

Acknowledgments

This work was supported by the National Key R&D Program of China (2022YFB4200101) and the National Natural Science Foundation of China (11834011, 11974242).

Appendix A. Supplementary data

Supplementary data to this article can be found online at https://doi.org/10.1016/j.energy.2024.132216.

References

[1] Rehman Au, Nadeem M, Usman M. Passivated emitter and rear totally diffused: PERT solar cell-an overview. Silicon 2022;15(2):639–49. https://doi.org/10.1007/s12633-022-02050-6.
[2] Green MA. The passivated emitter and rear cell (PERC): from conception to mass production. Sol Energy Mater Sol Cells 2015;143:190–7. https://doi.org/10.1016/j.solmat.2015.06.055.
[3] Blakers A. Development of the PERC solar cell. IEEE J Photovoltaics 2019;9(3):629–35. https://doi.org/10.1109/jphotov.2019.2899460.
[4] Krauß K, Fertig F, Greulich J, Rein S, Preu R. biPERC silicon solar cells enabling bifacial applications for industrial solar cells with passivated rear sides. Phys Status Solidi A 2016;213(1):68–71. https://doi.org/10.1002/pssa.201532737.
[5] Dullweber T, Schulte-Huxel H, Blankemeyer S, Hannebauer H, Schimanke S, Baumann U, et al. Present status and future perspectives of bifacial PERC+ solar cells and modules. Jpn J Appl Phys 2018;57. https://doi.org/10.7567/jjap.57.08ra01. 08RA1-9.
[6] Guerrero-Lemus R, Vega R, Kim T, Kimm A, Shephard LE. Bifacial solar photovoltaics – a technology review. Renew Sust Energy Rev 2016;60:1533–49. https://doi.org/10.1016/j.rser.2016.03.041.
[7] Park H, Chang S, Park S, Kim WK. Outdoor performance test of bifacial n-type silicon photovoltaic modules. Sustainability 2019;11(22):6234. https://doi.org/10.3390/su11226234.
[8] China photovoltaic industry association (CPIA). http://www.chinapv.org.cn; 2023.
[9] International technology roadmap for photovoltaic (ITRPV). https://itrpv.vdma.org; 2022.
[10] Dullweber T, Kranz C, Peibst R, Baumann U, Hannebauer H, Fülle A, et al. PERC+: industrial PERC solar cells with rear Al grid enabling bifaciality and reduced Al paste consumption. Prog Photovolt 2016;24(12):1487–98. https://doi.org/10.1002/pip.2712.
[11] Dullweber T, Schmidt J. Industrial silicon solar cells applying the passivated emitter and rear cell (PERC) concept—a review. IEEE J Photovoltaics 2016;6(5):1366–81. https://doi.org/10.1109/jphotov.2016.2571627.
[12] Min B, Muller M, Wagner H, Fischer G, Brendel R, Altermatt PP, et al. A roadmap toward 24% efficient PERC solar cells in industrial mass production. IEEE J Photovoltaics 2017;7(6):1541–50. https://doi.org/10.1109/jphotov.2017.2749007.
[13] Lv Y, Zhuang YF, Wang WJ, Wei WW, Sheng J, Zhang S, et al. Towards high-efficiency industrial p-type mono-like Si PERC solar cells. Sol Energy Mater Sol Cells 2020;204:110202. https://doi.org/10.1016/j.solmat.2019.110202.
[14] Zhang D, Chen J, Jia R, Gao Z, Tao K, Wang L, et al. Texture engineering of monocrystalline silicon via alcohol-free alkali solution for efficient PERC solar cells. J Energy Chem 2022;71:104–7. https://doi.org/10.1016/j.jechem.2022.03.016.
[15] Richter M, Saint-Cast P, Dannenberg T, Zimmer M, Rentsch J. Impact of rear side roughness on optical and electrical properties of a high-efficiency solar cell. Energy Proc 2015;77:832–9. https://doi.org/10.1016/j.egypro.2015.07.118.
[16] Wu W, Zhang Z, Zheng F, Lin W, Liang Z, Shen H. Efficiency enhancement of bifacial PERC solar cells with laser-doped selective emitter and double-screen-printed Al grid. Prog Photovolt 2018;26(9):752–60. https://doi.org/10.1002/pip.3013.
[17] Chen W, Liu R, Zeng Q, Zhou L. Low cost multicrystalline bifacial PERC solar cells – fabrication and thermal improvement. Sol Energy 2019;184:508–14. https://doi.org/10.1016/j.solener.2019.04.033.
[18] Lu G, Zheng F, Wang J, Shen W. Thin Al2O3passivated boron emitter of n-type bifacial c-Si solar cells with industrial process. Prog Photovolt 2017;25(4):280–90. https://doi.org/10.1002/pip.2859.
[19] Sugiura T, Matsumoto S, Nakano N. Bifacial PERC solar cell designs: bulk and rear properties and illumination condition. IEEE J Photovoltaics 2020;10(6):1538–44. https://doi.org/10.1109/jphotov.2020.3013987.
[20] Yu J, Wang P, Chen K, Chen T, Su R, Wang L, et al. Improved bifacial properties of P-type passivated emitter and rear cell solar cells toward high mass production efficiency. Phys Status Solidi A 2021;218(14):2100059. https://doi.org/10.1002/pssa.202100059.
[21] Li B, Yu J, Wang P, He J, Su R, Wang L, et al. Suppression of potential-induced degradation in monofacial PERC solar cells with gradient-designed capping layer. Sol Energy 2021;225:634–42. https://doi.org/10.1016/j.solener.2021.07.067.
[22] Ma S, Tang HB, Li ZP, Kong XY, Shen WZ. Application of SiOxNy films in industrial bifacial PERC solar cells. Sol Energy Mater Sol Cells 2021;230:111199. https://doi.org/10.1016/j.solmat.2021.111199.
[23] Kuo TC, Kuo CR, Lee W-H. Improvements in the efficiency of p-type bifacial Si solar cells with a rear Cu electrode using galvanic replacement reactions. Sol Energy Mater Sol Cells 2022;234:111411. https://doi.org/10.1016/j.solmat.2021.111411.
[24] Zauner M, Muehleisen W, Holzmann D, Baumgart M, Oreski G, Feldbacher S, et al. Light guidance film for bifacial photovoltaic modules. Renew Energy 2022;181:604–15. https://doi.org/10.1016/j.renene.2021.09.069.
[25] Tang HB, Ma S, Lv Y, Li ZP, Shen WZ. Optimization of rear surface roughness and metal grid design in industrial bifacial PERC solar cells. Sol Energy Mater Sol Cells 2020;216:110712. https://doi.org/10.1016/j.solmat.2020.110712.
[26] Ding J, Zou S, Shen L, Choi J, Cui J, Yuan D, et al. Improvement of light trapping in bifacial PERC silicon solar cells by optimizing the rear surface morphology. ACS Appl Energy Mater 2022;5(5):5875–85. https://doi.org/10.1021/acsaem.2c00220.
[27] Raina G, Sinha S. A simulation study to evaluate and compare monofacial vs bifacial PERC PV cells and the effect of albedo on bifacial performance. Mater Today Proc 2021;46:5242–7. https://doi.org/10.1016/j.matpr.2020.08.632.
[28] Guo S, Walsh TM, Peters M. Vertically mounted bifacial photovoltaic modules: a global analysis. Energy 2013;61:447–54. https://doi.org/10.1016/j.energy.2013.08.040.
[29] Gu W, Li S, Liu X, Chen Z, Zhang X, Ma T. Experimental investigation of the bifacial photovoltaic module under real conditions. Renew Energy 2021;173:1111–22. https://doi.org/10.1016/j.renene.2020.12.024.
[30] Neves LA, Leite GC, MacKenzie RCI, Ferreira RAM, Porto MP. A methodology to simulate solar cells electrical response using optical-electrical mathematical models and real solar spectra. Renew Energy 2021;164:968–77. https://doi.org/10.1016/j.renene.2020.09.053.
[31] Sato D, Yamagata Y, Hirata K, Yamada N. Mathematical power-generation model of a four-terminal partial concentrator photovoltaic module for optimal sun-tracking strategy. Energy 2020;213:118854. https://doi.org/10.1016/j.energy.2020.118854.
[32] Liang TS, Pravettoni M, Deline C, Stein JS, Kopecek R, Singh JP, et al. Correction: a review of crystalline silicon bifacial photovoltaic performance characterisation and simulation. Energy Environ Sci 2019;12(1):427. https://doi.org/10.1039/c8ee90071j.
[33] Gu W, Ma T, Ahmed S, Zhang Y, Peng J. A comprehensive review and outlook of bifacial photovoltaic (bPV) technology. Energy Convers Manag 2020;223:113283. https://doi.org/10.1016/j.enconman.2020.113283. A comprehensive review and outlook of bifacial photovoltaic (bPV) technology. Energy Convers. Manage. 2023, 113283.et al.
[34] Raina G, Sinha S. A holistic review approach of design considerations, modelling, challenges and future applications for bifacial photovoltaics. Energy Convers. Manage. 2022;271:116290. https://doi.org/10.1016/j.enconman.2022.116290.
[35] Du D, Qiao F, Guo Y, Wang F, Wang L, Gao C, et al. Photovoltaic performance of flexible perovskite solar cells under bending state. Sol Energy 2022;245:146–52. https://doi.org/10.1016/j.solener.2022.08.070.
[36] Du D, Gao C, Wang H, Shen W. Photovoltaic performance of bifacial perovskite/c-Si tandem solar cells. J Power Sour 2022;540:231622. https://doi.org/10.1016/j.jpowsour.2022.231622.
[37] Green MA. Self-consistent optical parameters of intrinsic silicon at 300K including temperature coefficients. Sol Energy Mater Sol Cells 2008;92(11):1305–10. https://doi.org/10.1016/j.solmat.2008.06.009.
[38] Boidin R, Halenkovič T, Nazabal V, Beneš L, Němec P. Pulsed laser deposited alumina thin films. Ceram Int 2016;42(1):1177–82. https://doi.org/10.1016/j.ceramint.2015.09.048.
[39] Beliaev LY, Shkondin E, Lavrinenko AV, Takayama O. Optical, structural and composition properties of silicon nitride films deposited by reactive radio-frequency sputtering, low pressure and plasma-enhanced chemical vapor deposition. Thin Solid Films 2022;763:139568. https://doi.org/10.1016/j.tsf.2022.139568.
[40] Lihong Gao FL, Lequime Michel. Exploitation of multiple incidences spectrometric measurements for thin film reverse engineering. Opt Express 2012;20:15734. https://doi.org/10.1364/OE.20.015734.
[41] Kranz C, Baumann U, Wolpensinger B, Lottspeich F, Müller M, Palinginis P, et al. Void formation in screen-printed local aluminum contacts modeled by surface energy minimization. Sol Energy Mater Sol Cells 2016;158:11–8. https://doi.org/10.1016/j.solmat.2016.06.039.
[42] https://www2.pvlighthouse.com.au.
[43] Garrod A, Ghosh A. A review of bifacial solar photovoltaic applications. Front Energy 2023;17(6):704–26. https://doi.org/10.1007/s11708-023-0903-7.